Supplementary Material

Study of *E. coli* Hfq's RNA annealing acceleration and duplex destabilization activities using substrates with different GC contents

Martina Doetsch[1], Sabine Stampfl[1], Boris Fürtig[1], Mads Beich-Frandsen[2], Krishna Saxena[3], Meghan Lybecker[1], Renée Schroeder*[1]

[1]Max F. Perutz Laboratories, Dept. for Biochemistry, Dr.-Bohrgasse 9, 1030 Vienna, Austria
[2]Max F. Perutz Laboratories, Dept. of Structural and Computational Biology, Dr.-Bohrgasse 9, 1030 Vienna, Austria
[3]Institute for Organic Chemistry and Chemical Biology, Johann Wolfgang Goethe University, Max-von-Laue-Strasse 7, 60438 Frankfurt am Main, Germany

*To whom correspondence should be addressed. Tel: +43-1-4277-54690; Fax: +43-1-4277-9528; renee.schroeder@univie.ac.at

The authors wish it to be known that, in their opinion, the first two authors should be regarded as joint First Authors.

Current address: Sabine Stampfl, Vis Vitalis GmbH, Moosham 29, 5585 Unternberg, Austria

Boris Fürtig, Institute for Organic Chemistry and Chemical Biology, Johann Wolfgang Goethe University, Max-von-Laue-Strasse 7, D-60438 Frankfurt am Main, Germany

Information on used RNA substrates

Supplementary Table 1: Circular structure plots of predicted RNA secondary structures. Briefly, in circular structure plots the bases of an RNA are arranged in a circle and an arc is drawn between the involved bases for each predicted base-pair. G-C pairs are depicted in red, A-U pairs in blue and G-U pairs in green. Structures were computationally folded and ΔG-values calculated using mfold 3.2 (1,2). ΔG-values correspond to the most stable of the predicted structures.

J1 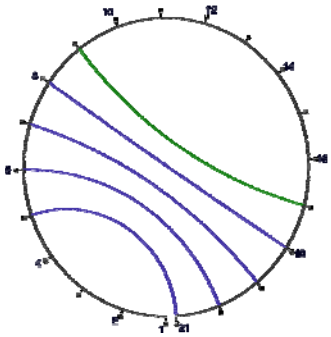 ΔG = 0.8 kcal/mol	J1h 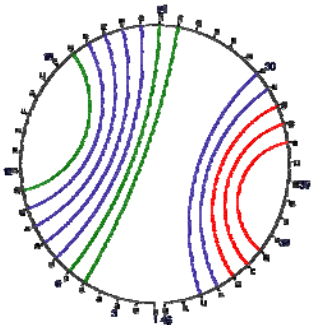 ΔG = -6.7 kcal/mol	M1 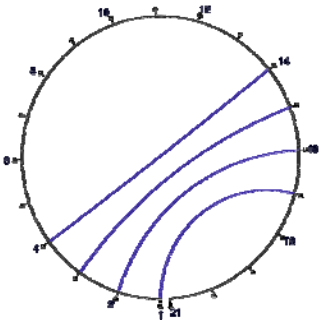 ΔG = 2.5 kcal/mol
J2 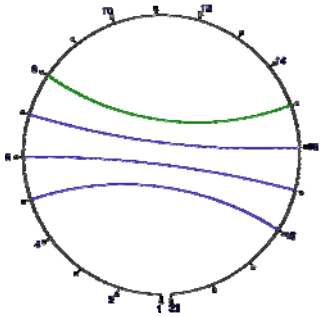 ΔG = 0.8 kcal/mol	J2h 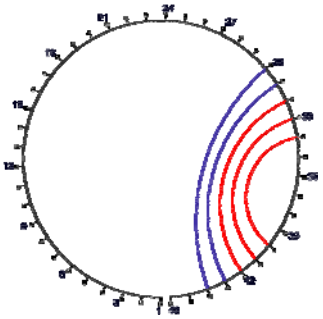 ΔG = -5.5 kcal/mol	M2 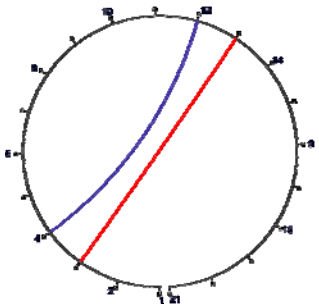 ΔG = 1.3 kcal/mol
J3 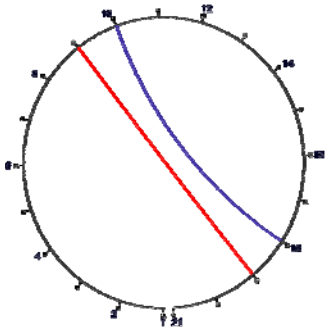 ΔG = 1.7 kcal/mol	J3h 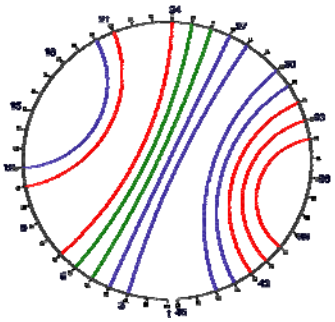 ΔG = -6.1 kcal/mol	M3 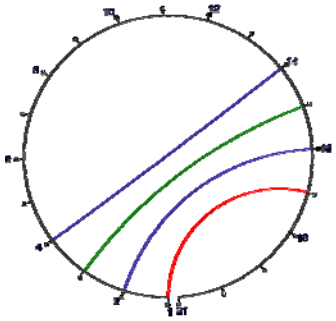 ΔG = 0.9 kcal/mol

Supplementary Table 1: Continued.

J4 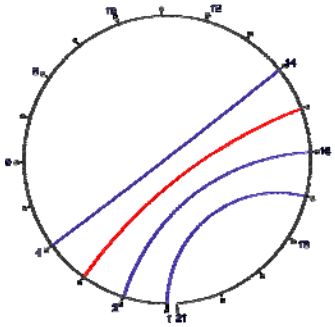 ΔG = 1.0 kcal/mol	J4h 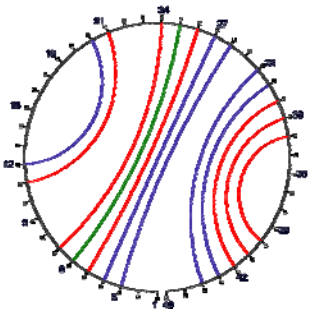 ΔG = -7.3 kcal/mol	M4 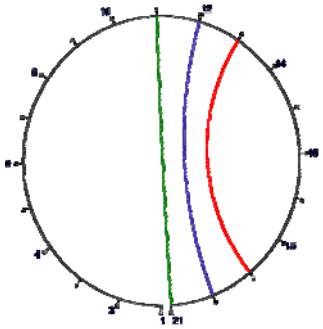 ΔG = 0.8 kcal/mol
J6 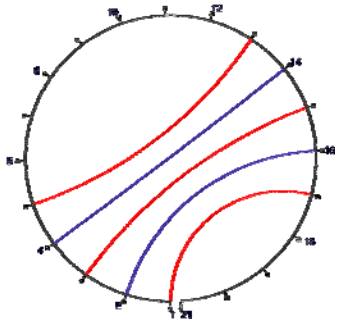 ΔG = -6.4 kcal/mol	J6h 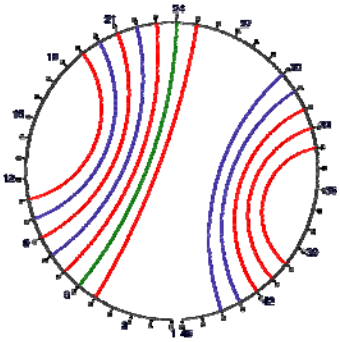 ΔG = -15.0 kcal/mol	M6 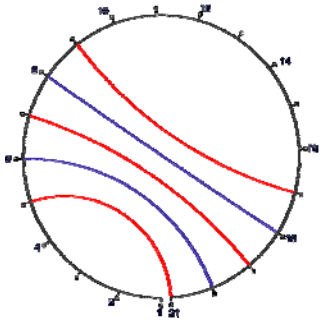 ΔG = -5.2 kcal/mol

FRET-based annealing and strand displacement assay

We consider the bimolecular reaction

$$A + B \rightarrow C$$

(the reaction rate for the back reaction can be neglected as it is considerably smaller than the rate of the forward reaction when using 21 base-pair long duplexes).
Assuming equimolarity for A and B, the reaction velocity is described by:

$$\frac{d[C]}{dt} = k \cdot [A] \cdot [B] = k \cdot [A]^2 = k \cdot ([A]_{t=0} - [C])^2 .$$

At very small time points t (for which $k_{obs, ann}$ is determined), [C] is negligible and thus the reaction velocity is directly proportional to $([A]_{t=0})^2$.
We measured observed annealing rate constants for initial RNA single-strand concentrations between 1 and 100 nM. The concentration dependency of $k_{obs, ann}$ on $([A]_{t=0})^2$ can be fitted to a linear equation (Supplementary Figure 1).

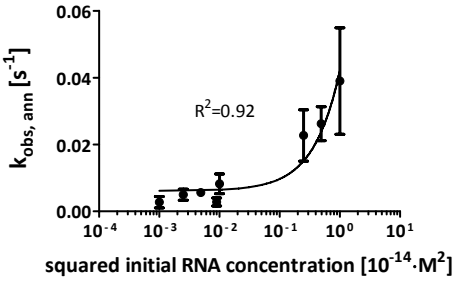

Supplementary Figure 1: Dependency of $k_{obs, ann}$ on the initial RNA concentration (JM1 RNA). Fitting of the data to the equation $k_{obs, ann} = a + b \cdot ([A]_{t=0})^2$ yields an R^2 of 0.92 (Note the logarithmic scale of the x-axis).

The Hfq-catalyzed annealing acceleration increases with increasing Hfq concentrations until it reaches a plateau at $Hfq_6 \approx$ 75-100 nM (Supplementary Figure 2).

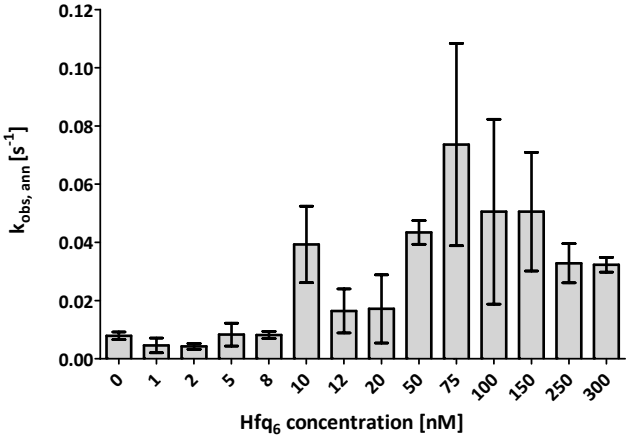

Supplementary Figure 2: Dependency of $k_{obs, ann}$ on Hfq_6 concentration. Hfq_6 annealing acceleration was measured using the 21R substrate, 5 nM initial RNA concentration and our standard buffer (50 mM Tris-HCl pH 7.5, 3 mM $MgCl_2$, 1 mM DTT). Values are means ± standard deviation for at least three measurements.

UV melting experiments

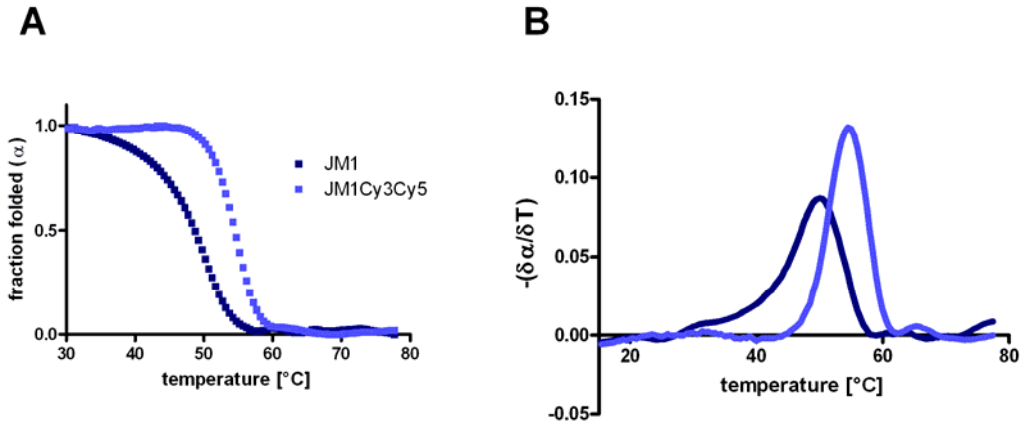

Supplementary Figure 3: 5'-labelling of an RNA duplex with Cy-dyes increases its stability. (A) Fraction of double-strands α = folded fraction/(folded fraction + unfolded fraction) versus the temperature as determined at 260 nm in UV melting experiments using the double-stranded RNAs JM1 (dark blue) and Cy5-J1/Cy3-M1 (light blue). **(B)** First derivatives of the data presented in (A).

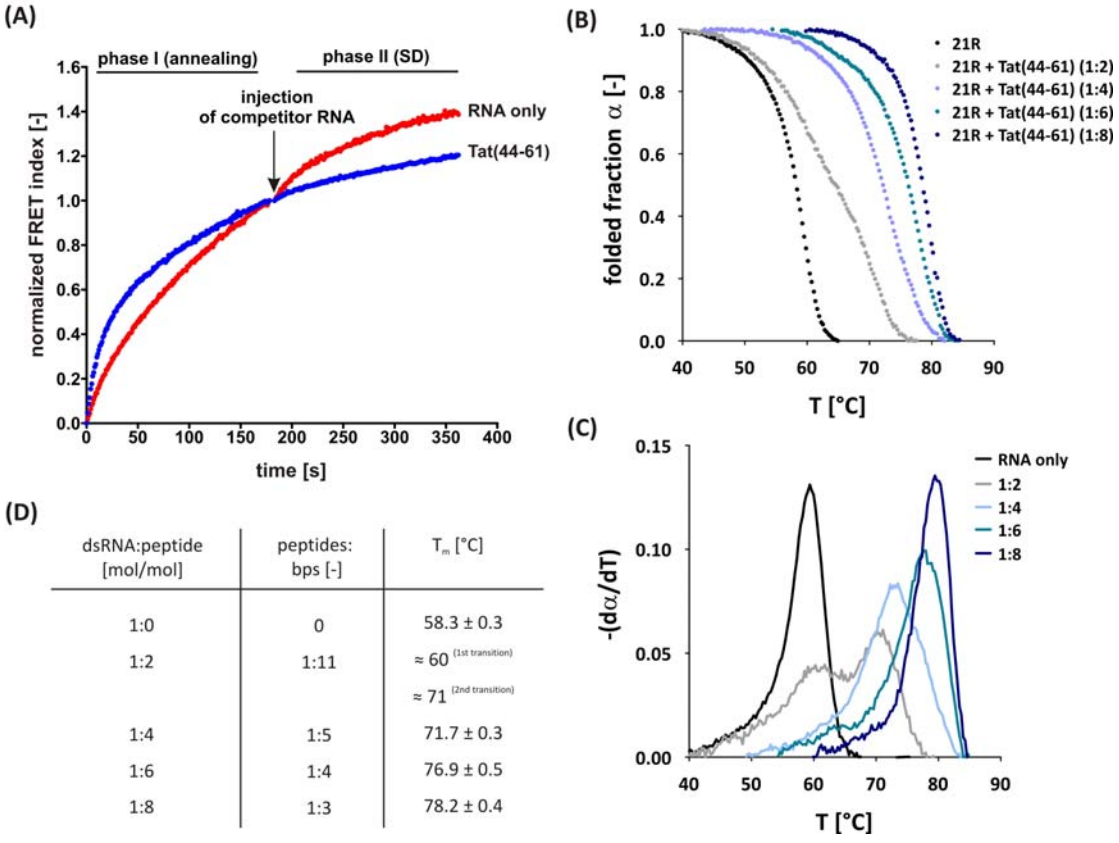

(D)

dsRNA:peptide [mol/mol]	peptides: bps [-]	T_m [°C]
1:0	0	58.3 ± 0.3
1:2	1:11	≈ 60 (1st transition)
		≈ 71 (2nd transition)
1:4	1:5	71.7 ± 0.3
1:6	1:4	76.9 ± 0.5
1:8	1:3	78.2 ± 0.4

Supplementary Figure 4: The Tat peptide accelerates annealing of complementary RNAs and stabilizes double-stranded RNAs. (A) In the FRET-based annealing and strand displacement (SD) assay the Tat peptide accelerated annealing of the 21R RNA approximately 7-fold (phase I), but did not catalyze strand displacement (phase II). **(B)** Tat(44-61) increased the melting temperature of the double-stranded 21R RNA in a peptide concentration dependent way as shown with UV melting experiments. α = folded fraction/(unfolded fraction + folded fraction). **(C)** The negative first derivate of α indicates the breadth of the melting transition as well as the biphasic melting behavior at a peptide to base-pair ratio of 1:11. **(D)** Overview of the determined melting temperatures at different RNA to peptide ratios.

Binding data for Hfq and single- and double-stranded RNA

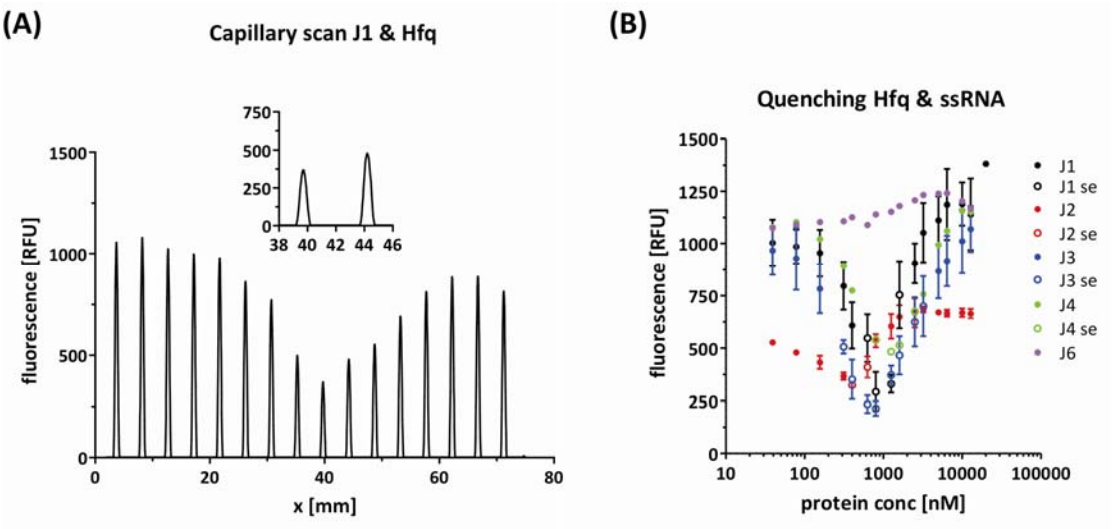

Supplementary Figure 5: Hfq binds single- and double-stranded RNAs as well as RNAs of different GC contents with different affinities as determined with microscale thermophoresis. (A) Representative capillary scan for the determination of capillary positions for the titration series with Cy5-labeled J1. The peak shapes indicate that no excessive Hfq binding to the capillaries or protein aggregation took place. Protein concentrations decrease with higher distances x. **(B)** Hfq quenches fluorescence of the Cy5- labeled single-stranded RNAs J1-4 in a concentration dependent fashion with the strongest quenching being around equimolar concentrations of RNA and Hfq_6. Fluorescence of Cy5-J6 is not quenched which indicates that this RNA does not interact with Hfq at the concentrations used.

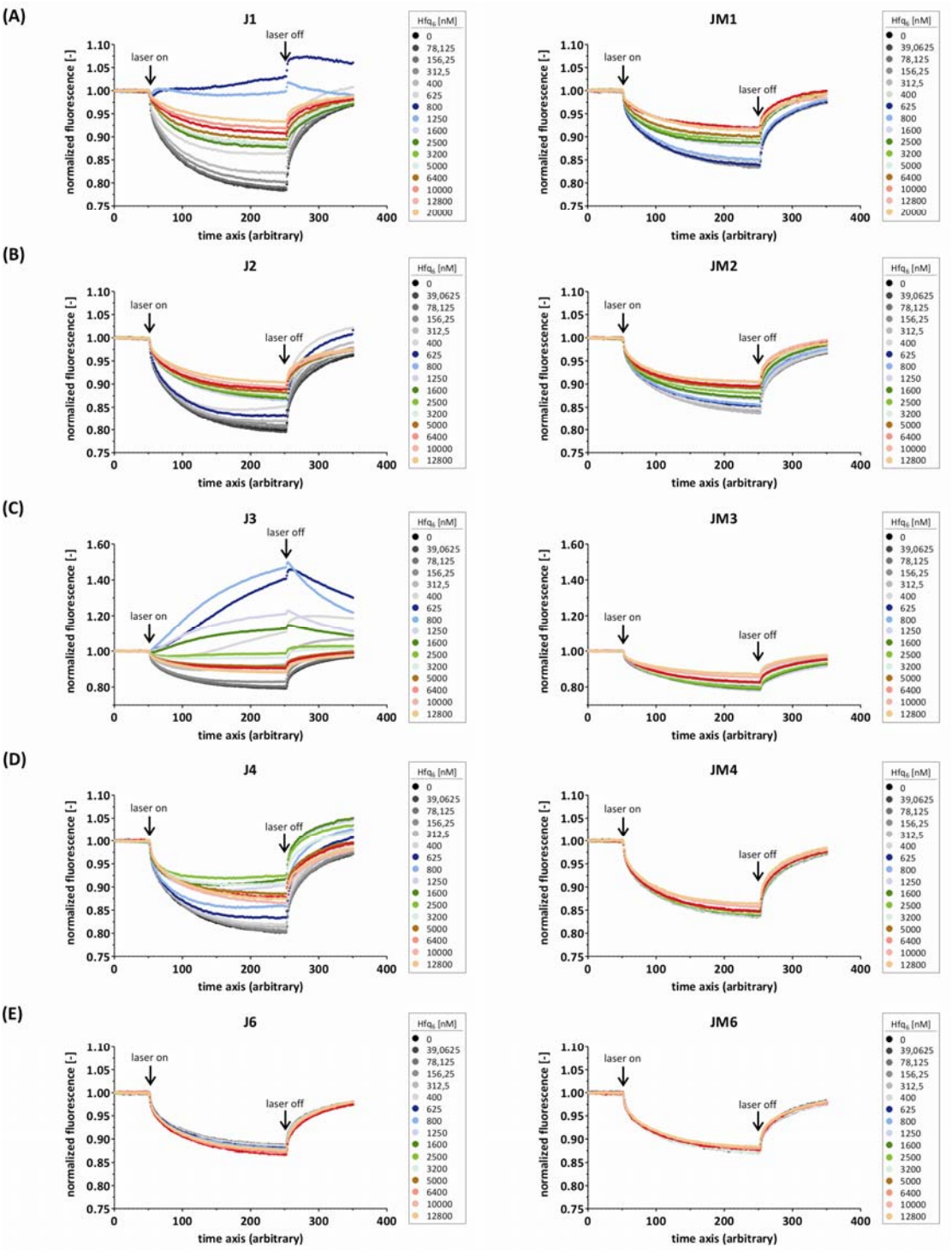

Supplementary Figure 6: Hfq binds single- and double-stranded RNAs as well as RNAs of different GC contents with different affinities as determined with microscale thermophoresis. MST experiments were carried out in the presence of different Hfq concentrations as indicated and (A) 1 µM Cy5-J1 or 1 µM Cy5-JM1, (B) 200 nM Cy5-J2 or 1 µM Cy5-JM2, (C) 1 µM Cy5-J3 or 1 µM Cy5-JM3, (D) 1 µM Cy5-J4 or 1 µM Cy5-JM4, (E) 1 µM Cy5-J6 or 1 µM Cy5-JM6. Time-dependent fluorescence signals were normalized to time point zero.

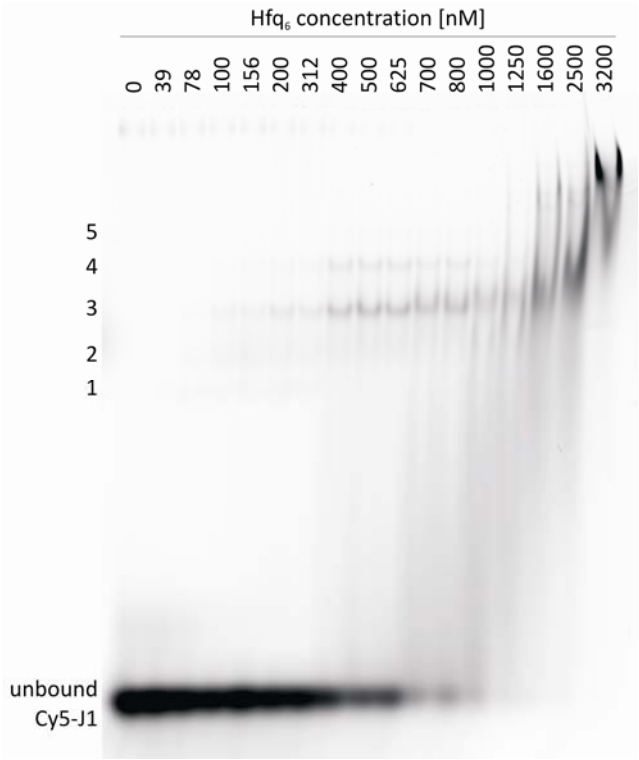

Supplementary Figure 7: Gel shift assay with Hfq and Cy5-J1 single-stranded RNA. 1 µM Cy5-labelled J1 RNA was incubated at room temperature for 15 minutes, with Hfq concentrations as indicated in Hfq binding buffer (50 mM Na-phosphate pH 8, 50 mM NaCl, 0.5 mM EDTA, 2 mM $MgCl_2$, 5% glycerol, 5 mM β-mercaptopethanol). RNA-Hfq complexes were separated at 50V and 4°C using 5% native PAGE (1xTBE). Fluorescent signals were scanned with a Typhoon TRIO scanner and bands were quantified with ImageQuant. At low Hfq concentrations distinct bands indicate more or less stable complexes with one or two Hfq molecules (shifts 1 to 5). The most intense of these shifts (shift 3) resembles only up to 6% of the total RNA loaded in the lane. Above 1000 nM Hfq_6 all RNA molecules are shifted, although no distinct bands are visible. The smears observed instead indicate transient Hfq:RNA interactions with binding on- and off-rates faster than the migration velocity. Quantification of the bands suggests a high cooperativity of Hfq interaction around equimolar Hfq-RNA concentrations. In line with this observation, Panja & Woodson (2012) (3) recently reported a concentration dependence of the Hfq hexamer/multimer to monomer ratio. They also hypothesized an RNA-stimulated Hfq hexamer formation as well as a stabilization of the hexamer through RNA binding.

Binding data for Tat(44-61) and 21R+ (ssRNA) and 21R (dsRNA)

In order to be able to compare Tat peptide binding to single-stranded versus double-stranded RNA, we applied standard techniques to determine K_Ds. However, due to the small size and high charge of the peptide as well as the small magnitude of the binding energy of the non-specific peptide-RNA interaction the most commonly used techniques to determine dissociation constants such as gel mobility shift assays, quenching methods, filter binding or isothermal calorimetry were not applicable to our system.

Gel shift assays as shown in Supplementary Figure 3 yielded only fuzzy RNA shifts of varying migration velocities so that an unambiguous K_D determination from these gels was impossible. Filter binding, in contrast, yielded reasonable binding curves, suggesting identical K_Ds and Hill factors for peptide binding to single- and double-stranded RNAs (Supplementary Figure 4). However, we believe that also filter binding might have a poor applicability to our system because the peptide size is slightly below the minimum protein molecular weight that can still be retained by the used nitrocellulose filter (Amersham Hybond™). As a rough estimate we suggest a K_D for Tat(44-61) binding to 21R+ or ds21R RNA in the low micromolar range.

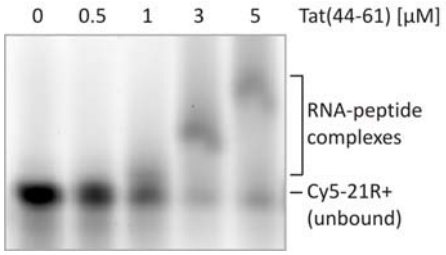

Supplementary Figure 8: Gel shift assay with Tat(44-61) and Cy5-labeled 21R+ single-stranded RNA. Binding reactions of 10 nM Cy5-21R+ RNA and Tat peptide concentrations as indicated were incubated in 50 mM Tris-HCl pH 7.5, 3 mM $MgCl_2$, 2 mM DTT and 10% Ficoll for 30 minutes at 37°C. Samples were run on a 16% polyacrylamide gel at 140 V and 4°C and fluorescence intensities were measured with a Typhoon Trio™ scanner. Despite buffer optimizations, peptide-RNA complexes were always diffuse and migrated with different velocities depending on the peptide concentration which hints at the binding of one RNA molecule through several peptide molecules. Importantly, the association/dissociation dynamics of the RNA-peptide complex were faster than the migration of the species within the gel (4). Additionally, a fraction of RNA remained unshifted even at high peptide concentrations.

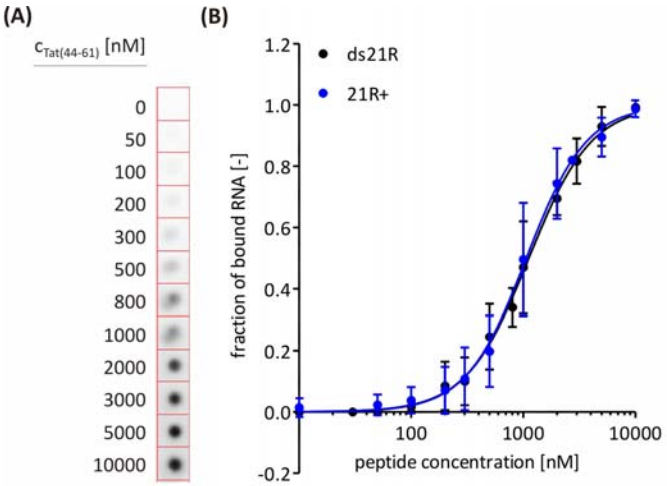

(C)

	K_D [nM]	h [-]
21R+ (ssRNA)	1065 ± 37	1.6 ± 0.1
ds21R	1121 ± 51	1.6 ± 0.1

Supplementary Figure 9: Filter binding assays indicate the same binding affinities of the Tat(44-61) peptide for both single-stranded and double-stranded RNA. (A) Representative image section of a filter with bound ^{32}P-RNA as visualized with phosphor imaging. Approximately 10 nM freshly kinased 21R+ single-stranded RNA or gel-purified ds21R RNA were titrated with Tat(44-61) in 1x binding buffer (50 mM Tris-HCl pH 7, 2 mM DTT, 6% glycerol) and incubated at room temperature for five minutes. A nitrocellulose filter was pre-equilibrated in 1x binding buffer and subsequently spanned into a Bio-Dot Microfiltration apparatus from BioRad. 90µl of the 100 µl reaction volume each were applied to the wells and filtered through with the help of a vacuum pump. Thus, peptide-bound RNA molecules stuck to the filter while unbound RNA was washed through. Wells were rinsed three times with 90 µl 1x binding buffer. The filter was dipped onto a paper towel in order to remove excessive liquid, wrapped into cling film and used to expose a phosphor imager screen. To avoid excessive RNA diffusion, phosphor imager screens were already scanned after two hours of exposure. **(B)** RNA binding to the filter was quantified using ImageQuant and the fraction of bound RNA was calculated as a function of peptide concentration. Mean curves and standard deviations were calculated from 4 to 16 data sets. **(C)** The data were fit to the following Hill equation for multiple binding sites:

$$fraction\quad bound = \frac{[peptide]^h}{K_D^h + [peptide]^h},$$

yielding dissociation constants K_D and Hill factors h.

A system that we believe to more accurately determine the dissociation constant of Tat peptide and single-stranded and double-stranded RNA was microscale thermophoresis (5). This technique is based on the fact that molecules migrate along a temperature gradient, usually away from the warmer temperature towards colder regions. The diffusion constant is thereby strongly dependent on the molecule's charge, size and hydration shell so that already smallest changes in the before mentioned factors are detectable with the method. Briefly, a small area of a capillary containing the sample is heated up via an infrared laser which induces a temperature gradient. The resulting movement and new equilibrium is monitored via the fluorescence of one labeled component. In our case, the RNA was 5'-Cy5-labeled and its concentration kept constant while the peptide was titrated.

The resulting curves from typical binding titrations with Tat(44-61) and ds21R dsRNA or 21R+ ssRNA are shown in Supplementary Figures 5 and 6. The binding buffer had been optimized in order to circumvent any peptide sticking to the capillaries or aggregation of peptide in bound or unbound form which would result in

an inhomogeneous distribution of molecules and thus bias the determined binding curves. The success of the buffer optimization is apparent from the peak shapes of the fluorescence signal (Supplementary Figure 5A & 6A). Tat(44-61) quenched the fluorescent signal of both RNA molecules which can be explained by static quenching (6). Quenching of the fluorescent signal was stronger for the dye attached to the single-stranded RNA (~90% at 25 µM peptide) than for the dye attached to the double-stranded RNA (~40% at 25 µM peptide) (Supplementary Figures 5B-C & 6B-C). Switching on the infrared laser to induce a temperature jump resulted in a movement of the RNA molecule from warm to cold temperatures (Supplementary Figures 5C & 6C). The equilibrium that adjusted itself during the period of heating was dependent on the peptide concentration added. Therefore, an influence of the RNA-peptide interaction on size, shape, charge and/or hydration shell of the RNA molecules can be concluded. For both RNAs (although much stronger in the case of single-stranded RNA) an additional and superimposing effect was visible in the fluorescence vs. time curves. The temperature jump induced a time-dependent increase in fluorescent signal that was counteracting the fluorescent depletion from the heated spot. As a consequence, the final fluorescence signal (after the laser was switched off) in samples with high peptide concentrations exceeded the original fluorescence (before the laser was switched on). The reason for this phenomenon remains speculative. The apparent irreversibility of the fluorescence increase might hint at a precipitation of peptide and thus a decreased peptide concentration. Indeed, Tat(44-61) tends to precipitate, although we never noticed a temperature dependence of this effect. We could also envision a strong electrophoretic movement of the (unbound) peptide which could be caused by a differential ion distribution along the temperature gradient (7) and which lowers the peptide concentration in the heated spot, leading to reduced fluorescence quenching. Because the original equilibrium is not reached, this process must take place on a time scale larger than the monitored one. Alternatively, the RNA/peptide binding properties might strongly depend on the temperature so that the laser-induced temperature difference induces an increased dissociation of RNA-peptide complexes.
Several indicators for binding strength can be delineated from the obtained fluorescence vs. time curves (Supplementary Figures 5C & 6C). As mentioned before, fluorescence quenching is an indicator for binding. Indeed, the quenching curves for both single-stranded and double-stranded RNA can be fitted to a Hill model for multiple binding sites:

$$F = A + B_{\max} \cdot \frac{[peptide]^h}{K_D^h + [peptide]^h}$$

(with F- fluorescence signal, A-offset, B_{max}- scaling factor, K_D-dissociation constant, h- Hill factor).

So-called thermophoresis $F_{norm,\ equil}$ compares the equilibrium fluorescence signals at high and low temperature with:

$$F_{norm,\ equil}[‰] = \frac{F_{hot,\ equil}}{F_{cold}} \cdot 1000$$

where F_{cold} is the fluorescence signal before the laser is switched on and $F_{hot,\ equil}$ is measured after the equilibrium state at the higher temperature has been reached. In contrast, the temperature jump (T jump) $F_{norm,\ T\ jump}$ is calculated using:

$$F_{norm,\,T\ jump}[‰] = \frac{F_{hot,\,T\ jump}}{F_{cold}} \cdot 1000$$

where $F_{hot,\ T\ jump}$ is measured right after the laser has been switched on, catching the fast RNA concentration change.
All three data sets can be fit to a Hill binding model for multiple binding sites:

$$Y = A + B_{\max} \cdot \frac{[peptide]^h}{K_D^h + [peptide]^h}$$

(with Y- fluorescence F or F_{norm}, A- offset, B_{max}- scaling factor, K_D- dissociation constant, h- Hill factor).
We found quenching to be only a rough indicator for binding affinity because with this method only peptide molecules are detected that bind to or in the direct vicinity of the fluorophore on the RNA's 5' end. Further peptide molecules bound to the RNA are not detected by this method which is due to their small size when compared to the RNA molecule. The thermophoresis signal $F_{norm,\ equil}$ is strongly falsified in the case of single-stranded 21R+ due to the mentioned superimposing effect while it should give reliable binding constants in the case of ds21R. Indeed, the dissociation constants and Hill factors determined with the thermophoresis signal and the T jump signal are identical for the double-stranded RNA which is expected for an unambiguous measurement (Supplementary Table 2) (Nanotemper Technologies MST Starting Guide- Monolith NT.115). The binding constants of Tat(44-61) to single-stranded RNA as determined from the thermophoresis curve and the T jump signal, however, differ strongly from each other. We consider the T jump signal to give the most reliable estimate of the dissociation constant and Hill factor because the superimposing effect is less prominent at early time points.
According to this signal, the K_Ds and Hill factors of peptide binding to both RNAs are identical within the error range (Supplementary Table 2).

Supplementary Table 2: Dissociation constants for Tat(44-61) binding to single-stranded 21R+ and double-stranded ds21R RNA as determined with MST.

	21R+		ds21R	
	K_D [µM]	h [-]	K_D [µM]	h [-]
T jump	6.3 ± 0.5	2.2 ± 0.3	7.4 ± 0.9	1.7 ± 0.3
Quenching	3.7 ± 0.2	2.9 ± 0.3	11 ± 2	1.3 ± 0.2
Thermophoresis	4.9 ± 0.2	3.7 ± 0.4	7.2 ± 0.5	1.7 ± 0.2

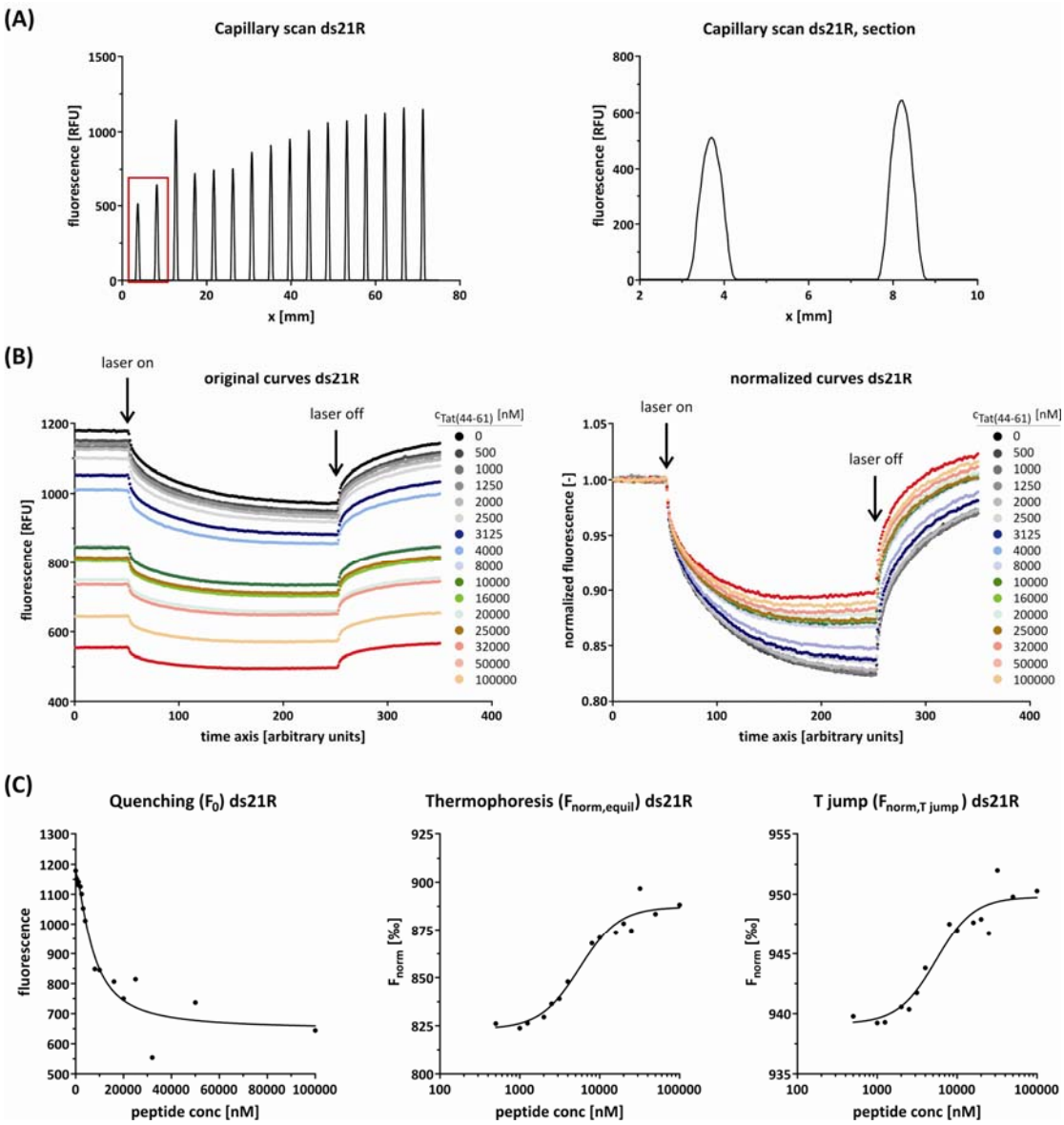

Supplementary Figure 10: Representative MST experiment estimating the binding of Tat(44-61) to Cy5-ds21R. (A) The preliminary capillary scan that is carried out to determine the exact position of the sample capillaries before each MST measurement. As can be judged from the peak shape, the samples are free of protein/RNA aggregation or excessive binding to the capillaries. Peptide concentrations are in reverse order (low x value = high Tat(44-61) concentration). **(B)** Original and normalized fluorescence curves of the MST measurements. The fluorescently labeled RNA (bound or unbound) moves from high temperatures to low temperatures as is indicated by the decrease in fluorescent signal after the infrared laser is switched on. Besides the thermophoretic movement of the RNA another effect (lift of fluorescent quenching by the peptide) is visible at higher peptide concentrations. **(C)** Peptide-induced fluorescent quenching, thermophoresis and temperature jump curves as delineated from the raw data in (B). All three data sets can be fit to a Hill binding model for multiple binding sites.

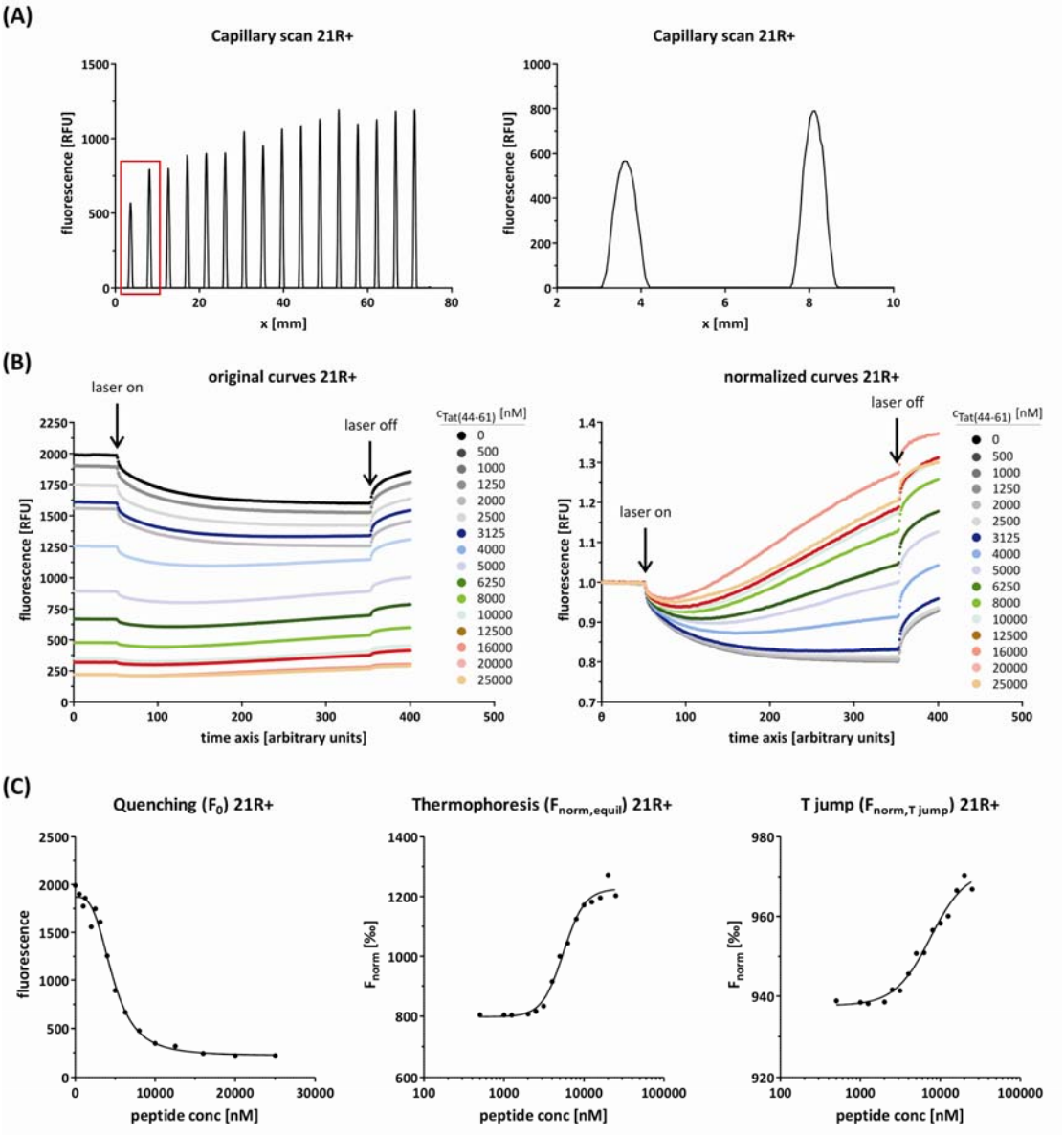

Supplementary Figure 11: Representative MST experiment estimating the binding of Tat(44-61) to Cy5-21R+ (single-stranded RNA). (A) The preliminary capillary scan that is carried out to determine the exact position of the sample capillaries before each MST measurement. As can be judged from the peak shape, the samples are free of protein/RNA aggregation or excessive binding to the capillaries, even at high peptide concentrations (low x values). **(B)** Original and normalized fluorescence curves of the MST measurements. The fluorescently labeled RNA (bound or unbound) moves from high temperatures to low temperatures as is indicated by the decrease in fluorescent signal after the infrared laser is switched on. At peptide concentrations above 4000 nM an additional effect (lift of the strong peptide-induced fluorescent quenching) is visible. **(C)** Peptide-induced fluorescent quenching, thermophoresis and temperature jump curves as delineated from the raw data in (B). All three data sets can be fit to a Hill binding model for multiple binding sites. However, due to the strong overlaying effect care must be taken when interpreting these binding curves.

References

1. Mathews, D.H., Sabina, J., Zuker, M. and Turner, D.H. (1999) Expanded sequence dependence of thermodynamic parameters improves prediction of RNA secondary structure. *J Mol Biol*, **288**, 911-940.
2. Zuker, M. (2003) Mfold web server for nucleic acid folding and hybridization prediction. *Nucleic Acids Res*, **31**, 3406-3415.
3. Panja, S. and Woodson, S.A. (2012) Hexamer to Monomer Equilibrium of E. coli Hfq in Solution and Its Impact on RNA Annealing. *J Mol Biol*, **417**, 406-412.
4. Cann, J.R. (1996) Theory and practice of gel electrophoresis of interacting macromolecules. *Anal Biochem*, **237**, 1-16.
5. Wienken, C.J., Baaske, P., Rothbauer, U., Braun, D. and Duhr, S. (2010) Protein-binding assays in biological liquids using microscale thermophoresis. *Nat Commun*, **1**, 100.
6. Walter, N.G. and Burke, J.M. (2000) Fluorescence assays to study structure, dynamics, and function of RNA and RNA-ligand complexes. *Methods Enzymol*, **317**, 409-440.
7. Hammack, A., Chen, Y.L. and Pearce, J.K. (2011) Role of dissolved salts in thermophoresis of DNA: lattice-Boltzmann-based simulations. *Phys Rev E Stat Nonlin Soft Matter Phys*, **83**, 031915.